ACS Catalysis

Research Article

Cite This: ACS Catal. 2019, 9, 8337−8345

pubs.acs.org/acscatalysis

Methane Pyrolysis with a Molten Cu−Bi Alloy Catalyst

Clarke Palmer,[†,#] Maryam Tarazkar,[‡,#] Henrik H. Kristoffersen,[§] John Gelinas,[†] Michael J. Gordon,[†] Eric W. McFarland,[*,†] and Horia Metiu[*,‡]

[†]Department of Chemical Engineering, University of California—Santa Barbara, Santa Barbara, California 93106-5080, United States

[‡]Department of Chemistry and Biochemistry, University of California—Santa Barbara, Santa Barbara, California 93106-9510, United States

[§]Department of Physics, Technical University of Denmark, 2800 Kgs., Lyngby 2800, Denmark

Supporting Information

ABSTRACT: Current methods of hydrogen production from methane generate more than 5 kg of CO_2 for every 1 kg of hydrogen. Methane pyrolysis on conventional solid heterogeneous catalysts produces hydrogen without CO_2, but the carbon coproduct poisons the catalyst. This can be avoided by using a molten metal alloy catalyst. We present here a study of methane pyrolysis using mixtures of molten Cu−Bi alloys as the catalyst. We find that molten Cu−Bi is an active catalyst, even though pure molten Bi and Cu are not. Surface tension measurements and constant-temperature ab initio molecular dynamics simulations indicate that the surface is enriched in Bi and that the catalytic activity is correlated with the concentration of Bi at the surface. Bader charge analysis indicates that bismuth donates charge to copper. In the most stable configuration of dissociated methane on these liquid surfaces, CH_3 binds to a bismuth surface atom and H to Cu. The energy barriers for the dissociative adsorption of methane, calculated using the nudged elastic band (NEB) method, are between 2.5 and 2.6 eV, depending on the binding site on the surface of the $Cu_{45}Bi_{55}$ alloy. The computed barriers are in rough agreement with the experimental apparent activation energy of 2.3 eV.

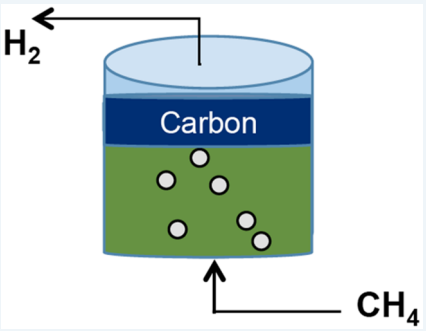

KEYWORDS: *methane, pyrolysis, hydrogen, coking, ab initio molecular dynamics, surface tension, bismuth/copper, molten alloy*

1. INTRODUCTION

The chemical industry produces annually more than 50 million tons of hydrogen, to be used primarily by ammonia, methanol, and oil industries. Associated with hydrogen production today is the generation of more than 300 million tons of CO_2, largely from the reforming of fossil hydrocarbons with steam. To produce even larger quantities of hydrogen from low-cost, abundant natural gas for use as a more sustainable fuel,[1−4] CO_2 coproduction can be avoided by methane pyrolysis:

$$CH_{4(g)} \rightarrow 2H_{2(g)} + C_{(s)} \qquad \Delta H^0 = 75\ \text{kJ/mol} \qquad (1)$$

The solid carbon coproduct can be transported and stored permanently in most locations far easier and cheaper than CO_2 sequestration, and it may have some value if produced in modest quantities.

Performing this reaction homogeneously in the gas phase requires very high temperatures, and carbon removal can be costly.[5−9] Conventional solid catalysts, such as supported metals or oxides, are quickly deactivated by carbon deposition.[2,10,11] The catalyst may be reactivated by burning the carbon (decoking), which produces CO_2.

One can avoid carbon poisoning by using a liquid metal catalyst and contacting the methane with the catalyst in a bubble column reactor.[12−18] One can think of each methane-containing bubble as a small batch reactor in which the liquid at the surface of the bubble is a continuously renewed catalyst. The carbon formed by the reaction is trapped at the bubble−liquid interface, rises with the bubble, and is deposited at the surface of the liquid column. If the carbon dissolves in the melt, it will reach saturation and will precipitate and be segregated at the surface of the melt. The solid−liquid separation and removal of solid carbon can then be readily accomplished. Each new bubble is in contact with a clean liquid surface that is not contaminated by carbon. In this process, the liquid is a self-cleaning catalyst, and the process is a reactive-separation.

Because methane pyrolysis must be performed at high temperatures, the liquid catalyst must be a thermally stable molten salt or molten metal. There is no large-scale implementation of such a process, but various estimates[3,4,19,20] conclude that it might be competitive with steam methane reforming, if a carbon tax is imposed or if the carbon produced is valuable.

Several molten metal systems have already been examined, including Al and Al alloys with ∼3 wt % Ni,[12] Fe,[13] Sn,[13−17]

Received: May 3, 2019
Revised: July 25, 2019
Published: August 9, 2019

DOI: 10.1021/acscatal.9b01833
ACS Catal. 2019, 9, 8337−8345

and Pb.[14] Upham et al.[18] pointed out that metals that are good catalysts for methane activation (e.g., Pt, Ni, Pd) have very high melting points, while metals that melt easily (e.g., Sn, Bi, In, Sn, Ga) are not good catalysts. They proposed the use of molten metal catalysts consisting of solutions of active metals in a low-melting metal that serves as a solvent. They tested several molten metal alloys and found that the easy-to-melt metals are essentially inactive, but alloying improves their catalytic activity substantially; Ni dissolved in Bi had the best performance.

In the present work, the approach of Upham et al.[18] is extended to investigate the catalytic properties of molten Cu−Bi alloys for methane pyrolysis. We have found that the molten Cu−Bi alloy surfaces have higher activity for methane conversion than 27 mol % Ni−73 mol % Bi ($Ni_{0.27}Bi_{0.73}$), which was the most active catalyst reported in previous studies. In addition, Cu is cheaper than Ni.

In his pioneering work on catalysis by molten metals, Ogino[21,22] presented data that showed a correlation between the surface tension of a binary melt and its catalytic activity. It is likely that a noncasual correlation between catalytic activity and surface tension exists because both depend on surface composition. For this reason, we have measured the surface tension and used Butler's equations to calculate surface composition as a function of known bulk composition. The qualitative conclusion is that the CuBi surface is most active catalytically when it is enriched in Bi. This is surprising because pure Bi is inactive.

The measurements reported here have led to two unexpected conclusions. Neither molten Cu nor molten Bi is a good methane pyrolysis catalyst, but the mixture is the most active molten metal catalyst for methane pyrolysis found so far. In the concentration range in which the melt is most active, the surface is substantially enriched in Bi. A pure Bi melt has very low catalytic activity, which means that the chemical properties of the Bi atoms at the surface of the alloy are substantially modified by their interaction with Cu or Ni atoms.

In an attempt to understand these results, we have performed constant-temperature ab initio molecular dynamics (MD) calculations to simulate the structural and chemical properties of molten Cu−Bi alloys. We have calculated the pair distribution functions, the local concentration and the charge on Cu and Bi as one approaches the surface of the liquid, and the activation energy for methane dissociation at the liquid's surface. The lowest activation energy for the breaking of the C−H bond is obtained when the CH_3 radical binds to a surface Bi in a Cu−Bi alloy and H binds to Cu.

2. EXPERIMENTAL RESULTS

2.1. Materials. Molten metal alloys were prepared from solid metal shots. Copper shots (0.60−0.85 mm, >99.5%) and bismuth shots (0.60−4.75 mm, >99.9%) were purchased from Sigma-Aldrich and used as received. Nickel shots (8−18 mm, >99.8%) were purchased from Rotometals and used as received. The reactors were made from either quartz or alumina.

2.2. Surface tension and surface compositions. In situ surface tension measurements were made using the maximum bubbling pressure method (see SI section 1). The surface tension was calculated by plotting the maximum bubble pressure versus depth (in the liquid column) where the bubble was formed. The surface tension was obtained from the Young−Laplace equation

$$P_{MAX} = P_{atm} + \rho g h + \frac{2\sigma}{R} \tag{2}$$

Here, P_{MAX} is the maximum bubble pressure at a certain depth h, σ is the surface tension, ρ is the density of the melt, g is gravitational acceleration, and R is the inner radius of the capillary tube through which the gas is fed.

The connection between the surface tension and the surface composition of the liquid metal alloy is given by Butler's thermodynamic equations[23,24] (see SI section 2)

$$\sigma = \sigma_i + \frac{RT}{A_i} \ln\left[\frac{\gamma_i^s x_i^s}{\gamma_i^B x_i^B}\right] \tag{3}$$

Here, σ is the surface tension of the alloy, σ_i is the surface tension of pure component i, A_i is the molar surface area of component i, γ_i is the activity coefficient of component i, and x_i is the composition of component i. Superscripts s and B indicate surface and bulk phases, respectively. The thermodynamic parameters present in this equation were taken from the FactSage thermochemical database.[25]

2.3. Catalytic Activity. To measure the catalytic activity per unit area of different molten metal alloys, we used a "screening reactor" that has been described in previous work[18] (see SI Figures S1 and S4). Briefly, a small ceramic crucible (8 mm OD, 5 mm height) is filled with the desired metal composition and melted in a large tube furnace under hydrogen and argon flow (7 sccm H_2 and 40 sccm argon). Single crucibles are then loaded into the bottom of a small quartz reactor (12 mm OD, 10 mm ID). A quartz gas delivery tube (8 mm OD, 1 mm ID) is inserted into the reactor. The outlet of the inlet tube is situated just above the surface of the crucible. For the measurements at 1000 and 1100 °C, 2.5 sccm of Ar/0.25 sccm of CH_4 and 5 sccm of Ar/0.5 sccm of CH_4 are flowed over the liquid metal surface, respectively. For the measurements at 1100 °C, 5 sccm of argon and 0.5 sccm of methane are flowed over the liquid metal surface. As soon as a stable conversion of methane is achieved, the reactor is quickly cooled. The crucible is replaced with a blank one, and the procedure is repeated (save the reduction step) in order to subtract any reactions occurring in the gas phase or on the walls of the quartz reactor.

One expects that the rate-limiting step in CH_4 pyrolysis is breaking of the C−H bond, and this suggests that the rate equation should be first-order in methane pressure; this is what is observed experimentally (see Figure 1). Methane consumption is calculated from methane conversion; the residence time (~0.7 s) and reactive surface area (~8.5 cm^2) are estimated from bubble rise velocities (~22 cm/s) and bubble sizes (~0.7 cm).

The Arrhenius plot of the rate constant extracted from the first-order rate law is shown in Figure 2.

Measurement of the activation energy was performed between 850 and 980 °C for methane conversions < 10% to minimize the back reaction and to allow us to assume a constant methane concentration in the effective rate equation

$$\frac{d[CH_4]}{dt} = -k[CH_4] \tag{4}$$

The conversion was calculated from the inlet and outlet concentrations of methane. The calculation of the rate constant used the estimated residence time of 0.7 s. The pyrolysis mechanism in a bubble column reactor is extremely

DOI: 10.1021/acscatal.9b01833
ACS Catal. 2019, 9, 8337−8345

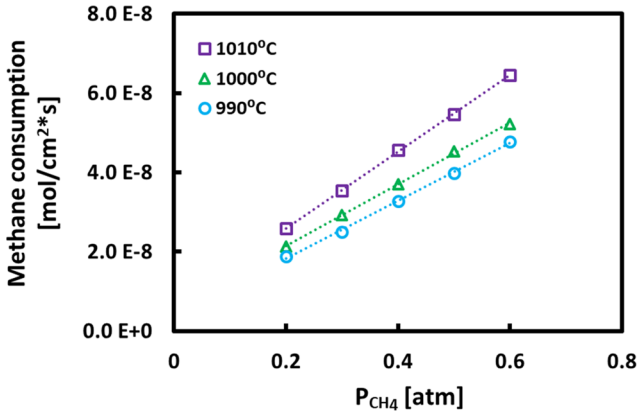

Figure 1. Methane consumption rate versus methane partial pressure in a 45 mol % Cu−55 mol % Bi bubble column reactor for different temperatures. The data were taken at a total pressure of 1 atm and a total bubbling flow rate of 10 sccm. The bubble size and residence time are estimated to be 0.7 cm and 0.7 s, respectively. The total liquid column height was ∼15 cm. Methane was supplemented with argon to adjust the methane partial pressure in the bubbles. The reactor head space was purged with 30 sccm of argon. Linearity in the curves confirms that the reaction order in methane is 1.

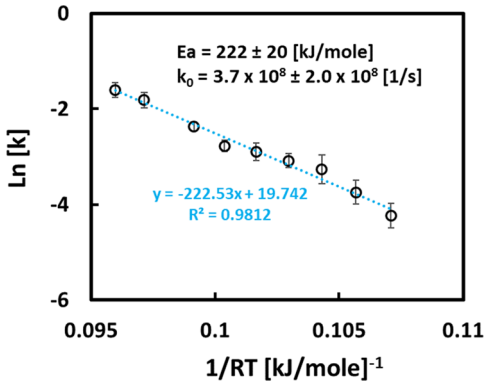

Figure 2. Arrhenius plot for the decomposition of methane at low (<10%) methane conversions in a 45 mol % Cu−55 mol % Bi melt.

complex, and the only virtue of this rate equation is that it fits the data and gives an apparent activation energy.

The concentration of "active metal" (e.g., Cu or Ni) in a Bi melt is limited by the phase diagram. There is, however, a wide enough solubility range at 1000 °C to allow a study of the dependence of the catalytic activity on the bulk concentration. In Figure 3, we compare the turnover frequency (TOF) for a molten Cu−Bi catalyst to that of molten Ni−Bi at 1000 °C, for different bulk concentrations.

The most striking feature of these data is that, while both pure Cu and pure Bi are poor pyrolysis catalysts at this temperature, the Cu−Bi mixture is very active. Its activity is slightly higher than that of Ni−Bi, which was the former champion. This is welcome news because the price of Ni is roughly 10 times higher than that of Cu, and Bi is relatively cheap.

The catalytic activity has a maximum at intermediate Cu−Bi concentrations, a feature that has been observed for other alloys.[18] This same trend is not seen for the Ni−Bi melts in Figure 3, perhaps because the low solubility of Ni in Bi at the working temperature prevented us from reaching the concentration at which the performance was maximum.

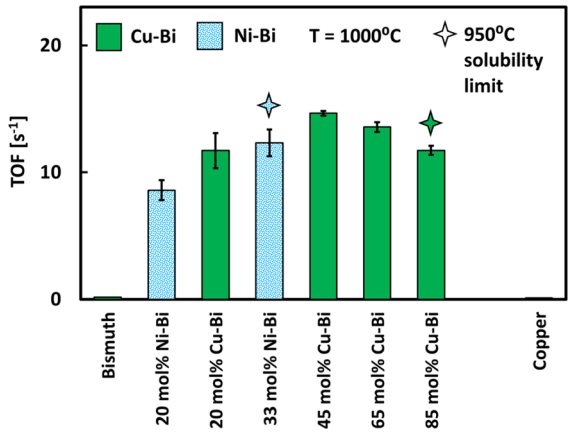

Figure 3. TOF of methane pyrolysis catalyzed by liquid Ni−Bi alloys, Cu−Bi alloys, pure bismuth at 1000 °C, and pure copper at 1100 °C. Methane (0.25 sccm) and argon (2.5 sccm) were flowed over a controlled surface area of 0.39 cm^2. Conditions at the solubility limit at 950 °C are indicated by the stars.

2.4. Activity Dependence on Surface Concentration.

To investigate the surface composition of molten Cu−Bi alloys as a function of the bulk composition, we performed surface tension measurements using the maximum bubbling pressure method (see SI section 1 for details). Figure 4 shows the results of our measurements, together with those of Oleksiak[26] and Birchumshaw,[27] and the values predicted by the Butler equation at 1000 °C (the Butler equation is reviewed in SI section 2).

Figure 4a shows that the maximum bubbling pressure method measurements of surface tension obtained in this work are consistent with values reported in the literature. The accurate measurements for the pure metals suggest that there are no impurities present, which typically segregate to the liquid surface and can decrease measured surface tension values compared to the values for the pure metals. The data show that bismuth dissolved in molten copper acts as a surfactant; the addition of a small amount of Bi substantially lowers the surface tension of liquid Cu, and the surface is enriched in Bi. Adding Bi to increase the molar fraction beyond ∼0.1 no longer affects the surface tension. The preferential surface enrichment with Bi is corroborated by our DFT calculations. Similar surface enrichment in one component, namely, the lower-surface-tension component, has been seen for other binary liquid metal alloys.[28−32]

Figure 4b shows that the precipitous drop of surface tension upon addition of Bi is accompanied by a substantial increase of bismuth molar fraction at the surface of the liquid. The surface bismuth composition is approximated by calculations based on the Butler equation (black curve, Figure 4b). Surface bismuth concentration correlates with the TOF for pyrolysis, as can be seen in Figure 4b. The catalyst is most active at bulk concentrations for which the concentration of bismuth at the surface is highest (Figure 4b). The TOF curve has a plateau at the same bulk concentration as the surface concentration.

We summarize these unexpected findings as follows. When the bulk Bi molar fraction is between 0.1 and 0.8, (a) the concentration of Bi at the surface is high (a molar fraction of ∼0.9) and constant, (b) the TOF for pyrolysis is high and constant, and (b) the TOF for pyrolysis is high and constant. The TOF is practically zero for pure Bi and pure Cu.

DOI: 10.1021/acscatal.9b01833
ACS Catal. 2019, 9, 8337−8345

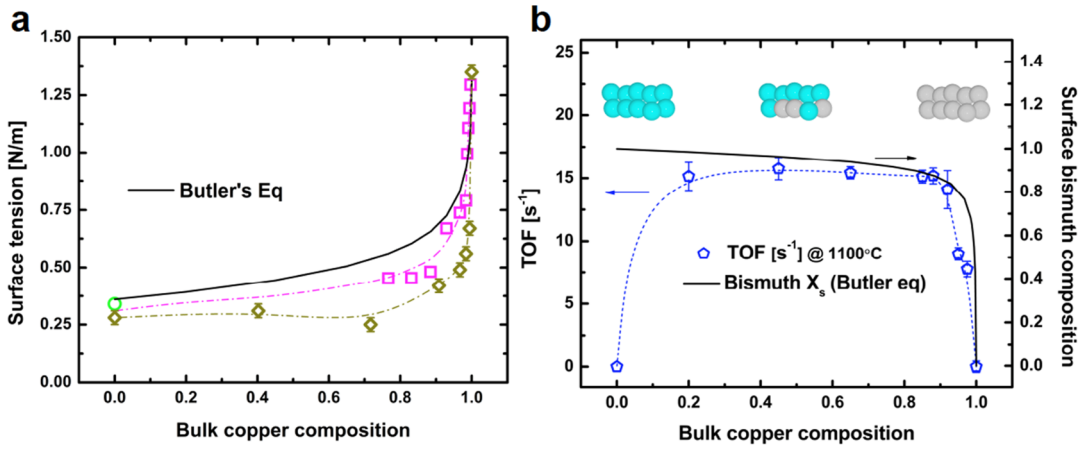

Figure 4. (a) Surface tension of Cu−Bi alloys versus the copper mole fraction in the bulk. Data from ref 26 (pink squares), ref 27 (green circle), and our measurements (diamonds). (b) Methane TOF for Cu−Bi alloys at 1100 °C (⬠) and surface bismuth composition versus bulk copper composition from the Butler equation (—). Dotted lines are only to guide the eye. [Inset in (b)] Aqua spheres qualitatively represent Bi atoms, and gray spheres qualitatively represent Cu atoms.

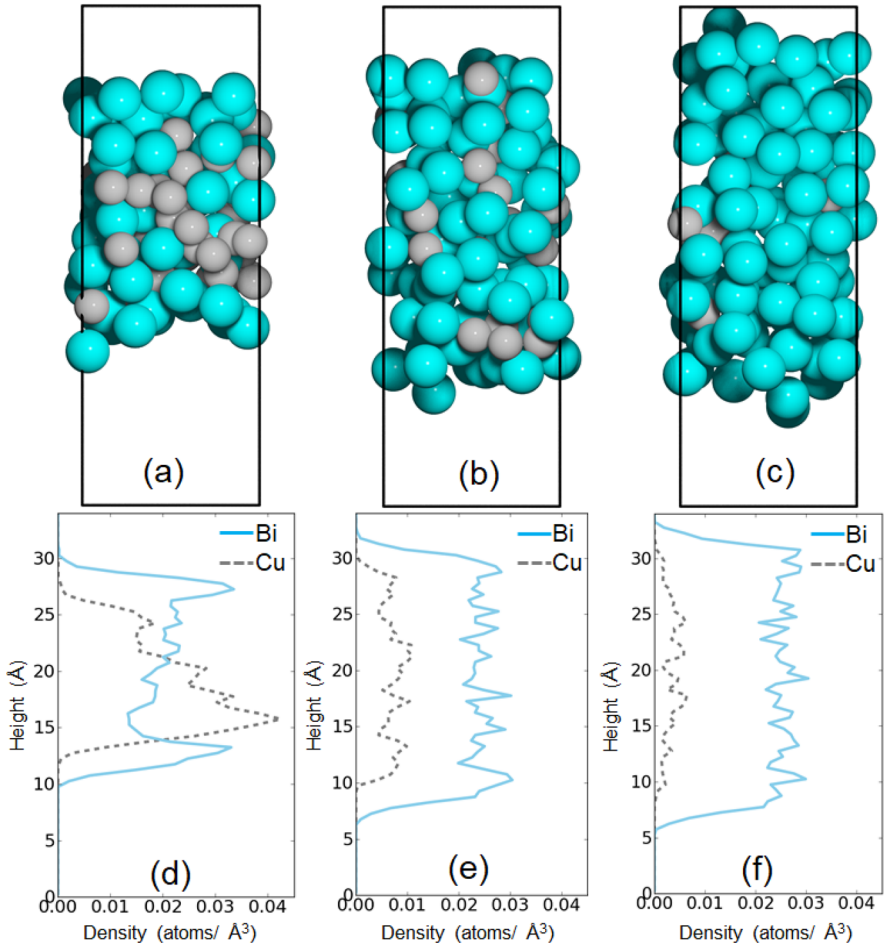

Figure 5. Snapshots of Cu−Bi melt systems after 12 ps of MD simulations for (a) $Cu_{45}Bi_{55}$, (b) $Cu_{20}Bi_{80}$, and (c) $Cu_{10}Bi_{90}$. (d−f) Average concentration (number of atoms per cubic Angstrom) of Bi and Cu atoms as a function of the coordinate perpendicular to the slab of liquid.

3. SIMULATIONS

3.1. Constant-Temperature Molecular Dynamics. The properties of the molten Cu−Bi alloys were investigated using ab initio, constant-temperature MD simulations,[33−35] as implemented in the VASP software package.[36−39] The energy in these simulations was provided by density functional theory (DFT), using a plane wave basis set with a 350 eV energy cutoff and a (2 × 2 × 1) Monkhorst−Pack *k*-point grid to sample reciprocal space. The PBE functional[40] with D3 van der Waals correction[41] was used to approximate the exchange−correlation effects. The calculations used the projector augmented wave method[36,42] and included 5 valence electrons

DOI: 10.1021/acscatal.9b01833
ACS Catal. 2019, 9, 8337−8345

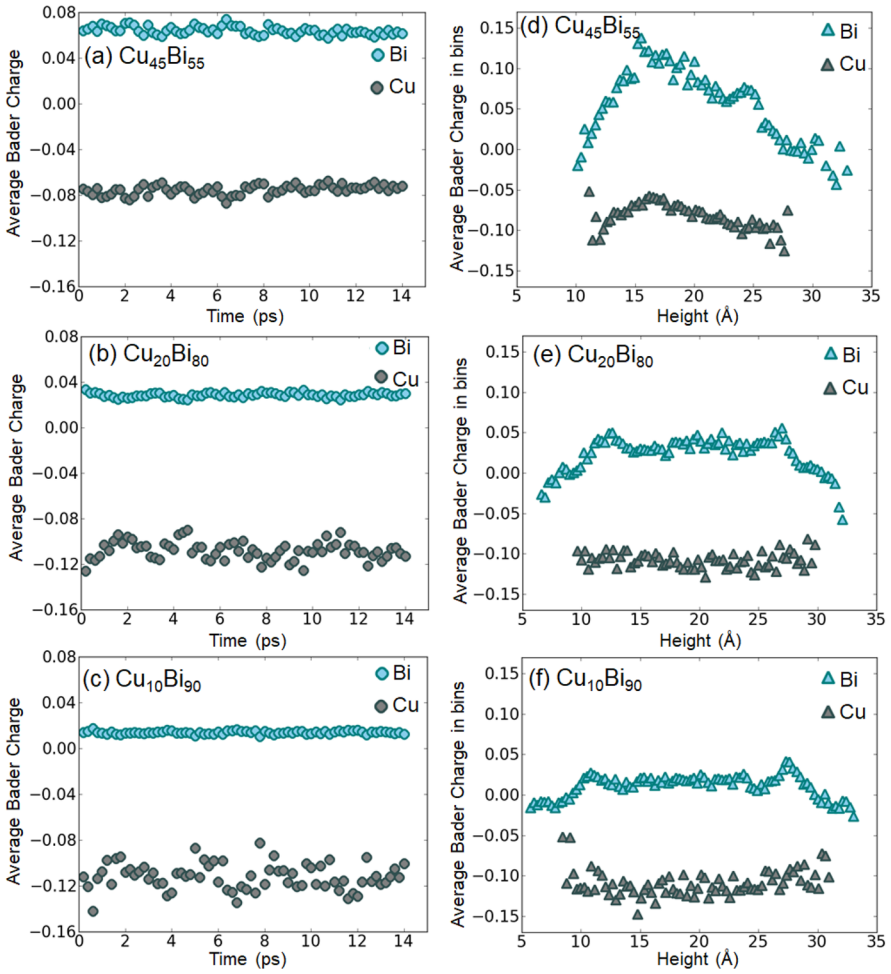

Figure 6. Time evolution of the average Bader charge on Cu and Bi atoms and the average Bader charge in different layers (bins) for molten (a,d) $Cu_{45}Bi_{55}$, (b,e) $Cu_{20}Bi_{80}$, and (c,f) $Cu_{10}Bi_{90}$ during an ab initio MD run.

for Bi, 11 electrons for Cu, 4 electrons for C, and 1 electron for H. The other electrons in the atoms were treated with the frozen core approximation. Spin-paired DFT calculations were performed in all calculations. Single-point spin-polarized calculations were performed to obtain Bader charges.[43−46] The energies obtained in spin-paired calculations were the same as those obtained with the spin-polarized case. For this reason, most of the calculations presented here were not spin-polarized.

3.2. Pair Correlation Functions. We used MD calculations to determine the pair distribution functions for molten $Cu_{45}Bi_{55}$, $Cu_{20}Bi_{80}$, and $Cu_{10}Bi_{90}$ alloys. The results are presented in SI Figure S5 and Table S2. The qualitative conclusion is that the system has a tendency for segregation: the neighborhood of a Cu atom has more Cu atoms than one would expect based on a random distribution. An excess of Bi is observed in the neighborhood of a Bi atom. There is no evidence in experiments that the system segregates into two phases. We emphasize that we used all atoms for calculating the pair correlation function; therefore, the result is a mean over the structure in the middle of the slab and that at the surface.

3.3. Concentration as a Function of the Distance from the Surface. We used the following procedure to calculate how a given quantity changes as a function of the distance to the surface of the layer. We divided the layer into a number of imaginary strips defined by planes parallel to the surface. We counted the number $n_\alpha(\mathrm{Bi};\, t)$ of Bi atoms and the number $n_\alpha(\mathrm{Cu},\, t)$ of Cu atoms, present at time t, in the strip α, whose center was located at z_α. The mean number of Bi atoms at a distance z_α from the surface was then given by eq 5:

$$\langle n(\mathrm{Bi};\, z_\alpha)\rangle_t = \frac{1}{t - t_0}\int_{t_0}^{t} n(\mathrm{Bi};\, z_\alpha,\, \tau)\, \mathrm{d}\tau \tag{5}$$

A similar formula was used to calculate $n_\alpha(\mathrm{Cu},\, t)$. Figure 5 shows how the concentration of Bi and Cu atoms varies across the liquid slab. In these simulations, we used a slab of liquid floating in vacuum, and the slab had two vacuum−liquid surfaces. If the slab was equilibrated and the statistics were satisfactory, the concentration variation with the distance across the slab should have been symmetrical with respect to the middle of the slab; the two liquid−vapor interfaces should have had the same time-averaged composition profile. This is true for the results shown in Figure 5e,f but not those in Figure 5d. We do not have an explanation for the asymmetry in Figure 5d, and we attribute it to insufficient sampling. The density profiles show surface segregation of Bi atoms for all bulk compositions; moreover, the outermost strips contain mostly Bi. The results for pure Cu and pure Bi are presented in SI Figure S6.

This is consistent with our experimental results and also with the rule that a low-surface-tension metal (Bi) preferentially

DOI: 10.1021/acscatal.9b01833
ACS Catal. 2019, 9, 8337−8345

segregates to the surface of a liquid alloy rather than the high-surface-tension component (Cu).[28−30,47]

3.4. Bader Charge Variation in the Direction Perpendicular to the Surface of the Liquid Slab. One of the interesting features of the experiments presented here is the mutual interaction between Cu and Bi: pure Cu and pure Bi are poor catalysts, yet the mixture has excellent activity. A possible explanation for this is that the modification in the chemistry is due to a change in the charge of the atoms when they are mixed to make an alloy. Because of this, we analyzed how the Bader charges on each atom depend on composition, on time, and on the distance of the atom from the surface.

Figure 6a−c shows the time evolution of the average Bader charge on Cu and Bi in the $Cu_{45}Bi_{55}$, $Cu_{20}Bi_{80}$, and $Cu_{10}Bi_{90}$ molten alloys. At any given time, we determined the Bader charge on each Bi atom and on each Cu atom, and the figure shows how the mean values of the charges change with time. Cu has a slight negative charge, and Bi is slightly positive as compared to the atoms in the gas phase. As the bulk concentration increases, Bi becomes slightly less positive. The mean charge fluctuates in time, but the fluctuations are small.

The dependence of the Bader charges as a function of the distance across the layer is more interesting (Figure 6d−f). Bi is less positive in the surface region than that in the bulk, and Cu is more positive. While the changes in the absolute values of the Bader charges are small, they are significant. In parallel, we studied the Bader charge distribution of atoms in pure Bi and pure Cu, and the results are shown in SI Figure S7. Pure Bi atoms are less positive than the Bi atoms in Cu−Bi alloys. The atoms in pure Cu are charge-neutral at the surface and in the bulk.

3.5. Energy of Methane Dissociation on the Surface of a Molten CuBi Alloy. The mean energy in constant-temperature MD is given by

$$\langle E \rangle_t = \frac{1}{t - t_0} \int_{t_0}^{t} E(\tau)\, \mathrm{d}\tau \tag{6}$$

where $E(\tau)$ is the total energy at time τ, calculated by DFT. The time t_0 is large enough to ensure that the system has equilibrated and has "forgotten" its initial configuration (SI Table S1). Because this is a constant-temperature simulation, the energy fluctuates in time. $\langle E \rangle_t$ is a cumulative average, and therefore, the most reliable values are those obtained at the longest running time. The sum of the energy of CH_4 in the gas phase with the energy of the melt is used as a reference; this means that we set this energy equal to 0. We can do that because we are interested in reaction energies only. The time evolution of the energies is shown in SI Figure S8. It is clear that in all calculations the mean energy has stabilized and lost memory of the initial state of the system.

The reaction energies are summarized in Table 1 and SI Figure S8 for the $Cu_{45}Bi_{55}$ melt. The notation used in the table is designed to indicate the binding sites of the dissociation fragments. For example, CH_3−$Bi_{55}Cu_{45}$ (surface) + H−$Cu_{45}Bi_{55}$ means that CH_3 is bonded to a Bi atom at the surface of the liquid, while H binds to a Cu atom.

It is often suspected that the interaction of methane with a molten metal at these high temperatures produces CH_3 radicals in the gas phase. The third row in the table indicates that the formation of CH_3 radicals in the gas is energetically unfavorable (compared to having adsorbed CH_3). However, the energy difference is not very large, and this conclusion may change if the desorption entropy is taken into account. The desorption of a CH_3 radical increases the entropy substantially, mainly due to the fact that $CH_3(g)$ translates in three dimensions and the translation of adsorbed CH_3 is two-dimensional. This means that the free energy for desorption is lowered by the entropy contribution; including the entropy in calculations makes CH_3 desorption more likely.

Table 1. Internal Energies for Adsorption of Methane on $Cu_{45}Bi_{55}$ Melt and Production of *H and *CH_3 Species on the Surface or Desorption of CH_3 to the Gas Phase[a]

reactions	ΔE (eV)
$CH_4(g) + Cu_{45}Bi_{55}(l) \rightarrow CH_3{-}Bi_{55}Cu_{45} + H{-}Cu_{45}Bi_{5545}Bi_{55}$ (run 1)	1.78
$CH_4(g) + Cu_{45}Bi_{55}(l) \rightarrow CH_3{-}Bi_{55}Cu_{45} + H{-}Cu$ (run 2)	1.51
$CH_4(g) + Cu_{45}Bi_{55}(l) \rightarrow CH_3(g) + H{-}Cu_{45}Bi_{55}$	2.51

[a]Run 1 and run 2 correspond to two different initial states, in which *CH_3 is placed on Bi atoms on the surface at two different sites.

We note that upon desorption the entropy change lowers the desorption free energy, qualitatively. Therefore, we cannot decide, based on internal energy calculation alone, whether CH_3 desorbs in the gas phase or is further dehydrogenated on the surface.

Methane dissociation to form CH_3 bonded to Bi and H bonded to Cu has the lowest energy. To better understand the nature of the bonds to the surface, we monitored the evolution of the C−Bi, C−Cu, H−Bi, and H−Cu distances as a function of time. We recorded the distance to the nearest atom in the liquid, not the distance to a designated Bi or Cu atom. The results are shown in Figure 7. In Figure 7a, the Bi−H distance is fairly large and has large fluctuations, which indicates that hydrogen does not make a chemical bond with Bi. On the other hand, the H−Cu distance is small and fluctuates little, suggesting that a chemical bond is formed. In a movie of the evolution of the system, we observed that an H bound to a Cu atom at the surface tends to hop to another Cu atom and move into the bulk. We have not seen this happen with CH_3.

The fact that the lowest energy is obtained when H binds to Cu and CH_3 to Bi is qualitatively consistent with the fact that bismuth hydride, BiH_3, is less stable than copper hydride, and methyl bismuth seems to be more stable than methyl copper.

3.6. Different Binding Configurations of H and CH_3. In most calculations on catalysis by solids, the atoms at the solid surface have well-defined positions around which they undergo small-amplitude vibrations. Because of this and of the periodic nature of the surface, there are only a few sites for the fragments produced by dissociative adsorption. One can therefore place the fragments in several locations that have a well-defined and permanent structure, as long as the temperature is not very large. This is not the case when the surface is liquid because the surface atoms are mobile and form many configurations having a transient lifetime. In addition, the liquid atoms have higher mobility and can undergo larger displacements to accommodate the bonding "needs" of the dissociation fragments.

To explore a variety of binding configurations, we used the following procedure. We selected a configuration (at 12 ps) from a long MD run and froze the bottom 80% of the slab and optimized the atomic positions of the metal atoms in the remaining 20%. In this way, we created a "glassy" solid whose structure is similar to that of the liquid. We then placed the fragments (*H and *CH_3) at different sites on the surface and

DOI: 10.1021/acscatal.9b01833
ACS Catal. 2019, 9, 8337−8345

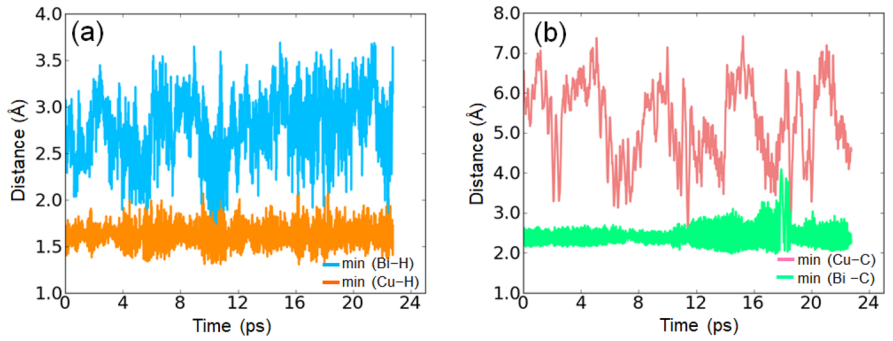

Figure 7. Minimum distances of (a) hydrogen (H) with Cu and Bi and (b) the carbon in CH_3 with Cu and Bi over time in a MD simulation of H and CH_3 on the surface of a $Cu_{45}Bi_{55}$ melt.

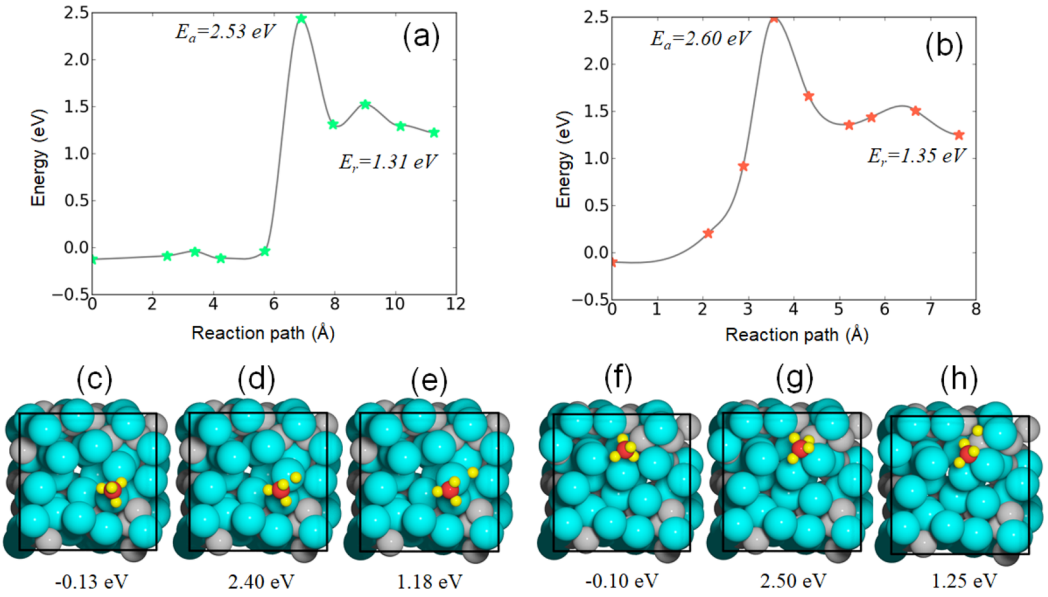

Figure 8. Potential energy surface for methane dissociation on the surface of $Cu_{45}Bi_{55}$, where (a) CH_3 and H were placed on a Bi atom and (b) CH_3 was placed on a Bi atom and H was placed between two Cu atoms. (c,f) Initial atomic configuration and physisorbed energy of methane on the surface of Cu–Bi. (d,g) Transition state energy and configuration for CH_4 dissociation. (e,h) Dissociated state consisting of CH_3* and H* species.

minimized the energy again. Various structures and their energies are shown in SI Figure S9. We find that the configuration in which both CH_3 and H are bridge-bonded with Bi has the lowest energy (hence, it is most likely to occur at equilibrium).

3.7. Activation Energy for Dissociative Adsorption of Methane. Calculation of the activation energy by using the nudged elastic band (NEB) method (for example) is quite common in the case of solid catalysts. Such calculations require that the system have well-defined initial and final states. This is not possible for a liquid surface where the surface atoms are mobile; different gas molecules colliding with a liquid surface will encounter different atomic configurations, and their activation energy for dissociative adsorption will be different.

We performed two NEB calculations for the two most stable final states for the adsorbed H and CH_3 on the $Cu_{45}Bi_{55}$ melt. Figure 8 shows the energy along the dissociation path. The activation energies are very similar for the two paths (2.53 and 2.60 eV). The experimental effective activation energy is 2.3 ± 0.2 eV. It is common to assume that the rate-limiting step in methane activation is breaking the C–H bond; therefore, the effective activation energy is essentially the activation energy for the dissociative adsorption of methane. Within the error of DFT, this is consistent with the results of our experiments.

Similarly, we calculated the activation energy of methane dissociation on a pure bismuth surface. The variation of the energy along the dissociation path, for the two most stable final configurations, is shown in Figure 9. The energies of the initial adsorbed methane molecule were −0.23 and −0.22 eV for the two configurations that we studied. The final states of the dissociated methane are similar to those of the $Cu_{45}Bi_{55}$ melt (Figure 7), and the dissociation energies were +1.24 and +1.28 eV. The calculated activation energies for methane dissociation on a pure bismuth surface were +2.80 and +2.90 eV (Figure 9a,b), which is markedly higher than those for the Cu–Bi alloy surfaces.

Previously, the calculated Bader charge on the transition metal atoms (assumed to be the active species) was correlated with the measured activity for methane pyrolysis: the smaller the negative charge, the higher the activity.[18] A similar trend is observed here. From the DFT-calculated Bader charges on Cu and Bi in Figure 6, it is clear that as the concentration of copper increases for the three compositions studied ($Cu_{10}Bi_{90}$,

DOI: 10.1021/acscatal.9b01833
ACS Catal. 2019, 9, 8337–8345

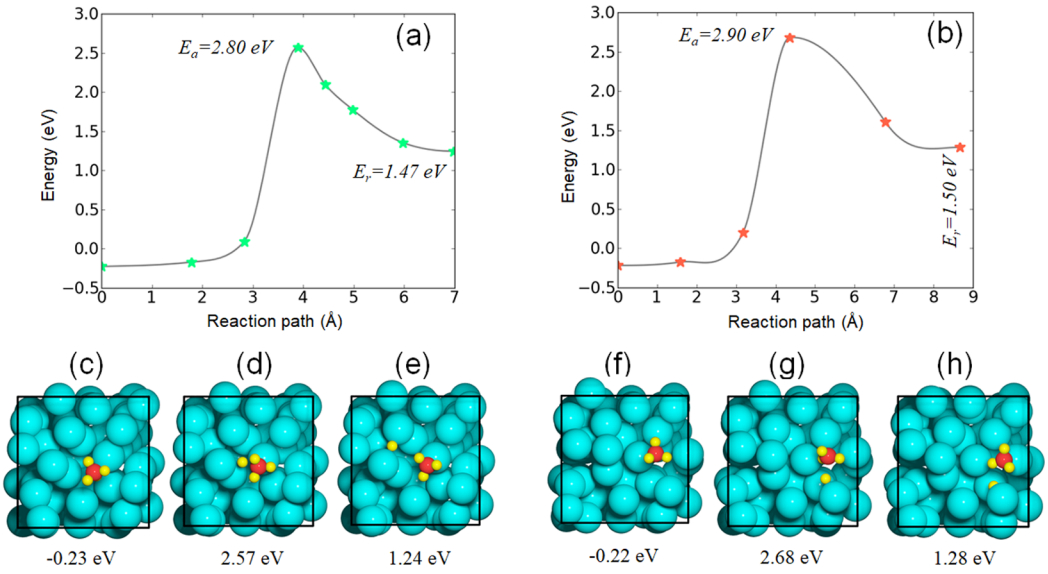

Figure 9. Potential energy surface for methane dissociation on the surface of Bi, where (a) *CH_3 and *H were placed between two Bi atoms and (b) *CH_3 and *H were placed on Bi atoms. (c,f) Initial atomic configuration and physisorbed energy of methane on the surface of Bi. (d,g) Transition state energy and configuration for CH_4 dissociation. (e,h) Dissociated state consisting of CH_3* and H* species.

$Cu_{20}Bi_{80}$, $Cu_{45}Bi_{55}$) the Bader charges on both Cu and Bi become more positive.

4. SUMMARY AND CONCLUSIONS

The surface metal compositions and electronic properties of molten Cu−Bi alloys have significant impact on their activity for methane activation and dehydrogenation. Experimental surface tension measurements confirm surface enrichment by bismuth in the molten Cu−Bi alloys. Similar enrichment was observed in the AIMD simulations. The measured activities as a function of metal composition suggest that at these surfaces electron-deficient bismuth species may be the active sites for methane activation. Because pure Bi has very low catalytic activity, this means that it is activated by the underlying copper. The electron-deficient bismuth sites promote the dissociation of methane, leaving the CH_3 group coordinated to a bismuth atom. The predicted methane activation energies of 2.5−2.6 eV on a $Cu_{45}Bi_{55}$ melt from NEB calculations are consistent with the experimentally measured effective activation energy of 2.3 eV.

■ ASSOCIATED CONTENT

Supporting Information

The Supporting Information is available free of charge on the ACS Publications website at DOI: 10.1021/acscatal.9b01833.

Surface tension measurements using the maximum bubbling pressure method; Butler equation derivation; reactors for catalytic activity measurements; choice of initial time for constant-temperature molecular dynamics; pair distribution functions; concentration as a function of the distance from the surface; Bader charge variation in the direction perpendicular to the surface of the liquid slab; binding sites of CH_3 and H on the surface; and activation energy for dissociative adsorption of CH_4 (PDF)

■ AUTHOR INFORMATION

Corresponding Authors

*E-mail: metiu@chem.ucsb.edu (H.M.).
*E-mail: ewmcfar@engineering.ucsb.edu (E.W.M.).

ORCID

Clarke Palmer: 0000-0001-7878-8318
Henrik H. Kristoffersen: 0000-0001-6943-0752
Michael J. Gordon: 0000-0003-0123-9649
Eric W. McFarland: 0000-0001-7242-509X
Horia Metiu: 0000-0002-3134-4493

Author Contributions

#C.P. and M.T. contributed equally.

Notes

The authors declare no competing financial interest.

■ ACKNOWLEDGMENTS

This work was primarily supported by the Energy & Biosciences Institute through the EBI-Shell program and the U.S. Department of Energy, Office of Science Basic Energy Sciences, Grant No. DE-FG03-89ER14048. We acknowledge the use of the Center for Scientific Computing supported by the California NanoSystems Institute and the Materials Research Science and Engineering Center (MRSEC) at UC Santa Barbara through NSF DMR 1720256 and NSF CNS 1725797.

■ REFERENCES

(1) Steinberg, M. The Hy-C Process (Thermal Decomposition of Natural Gas) Potentially the Lowest Cost Source of Hydrogen with the Least CO_2 Emission. *Energy Convers. Manage.* **1995**, *36*, 791−796.
(2) Holladay, J. D.; Hu, J.; King, D. L.; Wang, Y. An Overview of Hydrogen Production Technologies. *Catal. Today* **2009**, *139*, 244−260.
(3) Muradov, N. Z.; Vezirolu, T. N. From Hydrocarbon to Hydrogen−Carbon to Hydrogen Economy. *Int. J. Hydrogen Energy* **2005**, *30*, 225−237.
(4) Muradov, N. Low to near-Zero CO_2 Production of Hydrogen from Fossil Fuels: Status and Perspectives. *Int. J. Hydrogen Energy* **2017**, *42*, 14058−14088.

DOI: 10.1021/acscatal.9b01833
ACS Catal. 2019, 9, 8337−8345

(5) Olsvik, O.; Rokstad, O. A.; Holmen, A. Pyrolysis of Methane in the Presence of Hydrogen. *Chem. Eng. Technol.* **1995**, *18*, 349−358.
(6) Abanades, S.; Flamant, G. Solar Hydrogen Production from the Thermal Splitting of Methane in a High Temperature Solar Chemical Reactor. *Sol. Energy* **2006**, *80*, 1321−1332.
(7) Abanades, S.; Flamant, G. High-Temperature Solar Chemical Reactors for Hydrogen Production from Natural Gas Cracking. *Chem. Eng. Commun.* **2008**, *195*, 1159−1175.
(8) Abanades, S.; Tescari, S.; Rodat, S.; Flamant, G. Natural Gas Pyrolysis in Double-Walled Reactor Tubes Using Thermal Plasma or Concentrated Solar Radiation as External Heating Source. *J. Nat. Gas Chem.* **2009**, *18*, 1−8.
(9) Abánades, A.; Ruiz, E.; Ferruelo, E. M.; Hernández, F.; Cabanillas, A.; Martínez-Val, J. M.; Rubio, J. A.; López, C.; Gavela, R.; Barrera, G.; Rubbia, C.; Salmieri, D.; Rodilla, E.; Gutiérrez, D. Experimental Analysis of Direct Thermal Methane Cracking. *Int. J. Hydrogen Energy* **2011**, *36*, 12877−12886.
(10) Li, Y.; Li, D.; Wang, G. Methane Decomposition to CO_x-Free Hydrogen and Nano-Carbon Material on Group 8−10 Base Metal Catalysts: A Review. *Catal. Today* **2011**, *162*, 1−48.
(11) Choudhary, T. V.; Aksoylu, E.; Goodman, D. W. Nonoxidative Activation of Methane. *Catal. Rev.: Sci. Eng.* **2003**, *45*, 151−203.
(12) Oblad, A. G.; Milliken, T. G., Jr.; Boedeker, E. R. Production of Hydrogen and Carbon. U.S. Patent 2,760,847, 1956.
(13) Steinberg, M.; Dong, Y. Method for Converting Natural Gas and Carbon Dioxide to Methanol and Reducing CO_2 Emission. U.S. Patent 5,767,165, 1998.
(14) Serban, M.; Lewis, M. A.; Marshall, C. L.; Doctor, R. D. Hydrogen Production by Direct Contact Pyrolysis of Natural Gas. *Energy Fuels* **2003**, *17*, 705−713.
(15) Abánades, A.; Rathnam, R. K.; Geißler, T.; Heinzel, A.; Mehravaran, K.; Müller, G.; Plevan, M.; Rubbia, C.; Salmieri, D.; Stoppel, L.; Stückrad, S.; Weisenburger, A.; Wenninger, H.; Wetzel, T. Development of Methane Decarbonisation Based on Liquid Metal Technology for CO_2-Free Production of Hydrogen. *Int. J. Hydrogen Energy* **2016**, *41*, 8159−8167.
(16) Geißler, T.; Plevan, M.; Abánades, A.; Heinzel, A.; Mehravaran, K.; Rathnam, R. K.; Rubbia, C.; Salmieri, D.; Stoppel, L.; Stückrad, S.; Weisenburger, A.; Wenninger, H.; Wetzel, T. Experimental Investigation and Thermo-Chemical Modeling of Methane Pyrolysis in a Liquid Metal Bubble Column Reactor with a Packed Bed. *Int. J. Hydrogen Energy* **2015**, *40*, 14134−14146.
(17) Plevan, M.; Geißler, T.; Abánades, A.; Mehravaran, K.; Rathnam, R. K.; Rubbia, C.; Salmieri, D.; Stoppel, L.; Stückrad, S.; Wetzel, T. Thermal Cracking of Methane in a Liquid Metal Bubble Column Reactor: Experiments and Kinetic Analysis. *Int. J. Hydrogen Energy* **2015**, *40*, 8020−8033.
(18) Upham, D. C.; Agarwal, V.; Khechfe, A.; Snodgrass, Z. R.; Gordon, M. J.; Metiu, H.; McFarland, E. W. Catalytic Molten Metals for the Direct Conversion of Methane to Hydrogen and Separable Carbon. *Science* **2017**, *358*, 917−921.
(19) Steinberg, M. Fossil Fuel Decarbonization Technology for Mitigating Global Warming. *Int. J. Hydrogen Energy* **1999**, *24*, 771−777.
(20) Parkinson, B.; Matthews, J. W.; McConnaughy, T. B.; Upham, D. C.; McFarland, E. W. Techno-Economic Analysis of Methane Pyrolysis in Molten Metals: Decarbonizing Natural Gas. *Chem. Eng. Technol.* **2017**, *40*, 1022−1030.
(21) Ogino, Y. Catalysis by Molten Metals and Molten Alloys. *Catal. Rev.: Sci. Eng.* **1981**, *23*, 505−551.
(22) Ogino, Y. *Catalysis and Surface Properties of Liquid Metals and Alloys*; Marcel Dekker: New York, 1987.
(23) Butler, J. A. V. The Thermodynamics of the Surfaces of Solutions. *Proc. R. Soc. London, Ser. A* **1932**, *135*, 348−375.
(24) Tanaka, T.; Hack, K.; Hara, S. Calculation of Surface Tension of Liquid Bi-Sn Alloy Using Thermochemical Application Library ChemApp. *CALPHAD: Comput. Coupling Phase Diagrams Thermochem.* **2000**, *24*, 465−474.
(25) Bale, C. W.; Bélisle, E.; Chartrand, P.; Decterov, S. A.; Eriksson, G.; Gheribi, A. E.; Hack, K.; Jung, I. H.; Kang, Y. B.; Melançon, J.; Pelton, A. D.; Petersen, S.; Robelin, C.; Sangster, J.; Ende, M.-A. V. *FactSage Thermochemical Software and Databases*; Calphad, 2010−2016; Vol. *54*, pp 35−53.
(26) Oleksiak, B.; Łabaj, J.; Wieczorek, J.; Blacha-Grzechnik, A.; Burdzik, R. Surface Tension of Cu−Bi Alloys and Wettability in a Liquid Alloy−Refractory Material−Gaseous Phase System. *Arch. Metall. Mater.* **2014**, *59*, 282−286.
(27) Bircumshaw, L. L. CXXIV. The Surface Tension of Liquid Metals. Part II. The Surface Tension of Bismuth, Cadmium, Zinc, and, Antimony. *Philos. Mag.* **1927**, *3*, 1286−1294.
(28) DiMasi, E.; Tostmann, H.; Shpyrko, O. G.; Deutsch, M.; Pershan, P. S.; Ocko, B. M. Surface-Induced Order in Liquid Metals and Binary Alloys. *J. Phys.: Condens. Matter* **2000**, *12*, A209−A214.
(29) DiMasi, E.; Tostmann, H.; Shpyrko, O. G.; Huber, P.; Ocko, B. M.; Pershan, P. S.; Deutsch, M.; Berman, L. E. Pairing Interactions and Gibbs Adsorption at the Liquid Bi-in Surface: A Resonant X-Ray Reflectivity Study. *Phys. Rev. Lett.* **2001**, *86*, 1538−1541.
(30) Shpyrko, O. G.; Grigoriev, A. Y.; Streitel, R.; Pontoni, D.; Pershan, P. S.; Deutsch, M.; Ocko, B.; Meron, M.; Lin, B. Atomic-Scale Surface Demixing in a Eutectic Liquid Bi-Sn Alloy. *Phys. Rev. Lett.* **2005**, *95*, 106103.
(31) Lei, N.; Huang, Z.; Rice, S. A. Structure of the Liquid−Vapor Interface of a Sn:Ga Alloy. *J. Chem. Phys.* **1997**, *107*, 4051−4060.
(32) Ashkhotov, O. G.; Ashkhotova, I. B.; Aleroev, M. A.; Magkoev, T. T.; Bliev, A. P. Surface Properties of Sodium, Potassium, and Their Binary Alloys in the Liquid State. *Russ. J. Phys. Chem. A* **2017**, *91*, 1270−1272.
(33) Nosé, S. A Molecular Dynamics Method for Simulations in the Canonical Ensemble. *Mol. Phys.* **1984**, *52*, 255−268.
(34) Nosé, S. A Unified Formulation of the Constant Temperature Molecular Dynamics Methods. *J. Chem. Phys.* **1984**, *81*, 511−519.
(35) Nosé, S. A Molecular Dynamics Method for Simulations in the Canonical Ensemble. *Mol. Phys.* **2002**, *100*, 191−198.
(36) Kresse, G. J.; Joubert, D. From Ultrasoft Pseudopotentials to the Projector Augmented-Wave Method. *Phys. Rev. B: Condens. Matter Mater. Phys.* **1999**, *59*, 1758−1775.
(37) Kresse, G.; Hafner, J. Ab Initio Molecular-Dynamics Simulation of the Liquid-Metal−Amorphous-Semiconductor Transition in Germanium. *Phys. Rev. B: Condens. Matter Mater. Phys.* **1994**, *49*, 14251−14269.
(38) Kresse, G.; Furthmüller, J. Efficient Iterative Schemes for Ab Initio Total-Energy Calculations Using a Plane-Wave Basis Set. *Phys. Rev. B: Condens. Matter Mater. Phys.* **1996**, *54*, 11169−11186.
(39) Kresse, G. Ab Initio Molecular Dynamics for Liquid Metals. *J. Non-Cryst. Solids* **1995**, *192*−*193*, 222−229.
(40) Perdew, J. P.; Burke, K.; Ernzerhof, M. Generalized Gradient Approximation Made Simple. *Phys. Rev. Lett.* **1996**, *77*, 3865−3868.
(41) Grimme, S.; Antony, J.; Ehrlich, S.; Krieg, H. A Consistent and Accurate Ab Initio Parametrization of Density Functional Dispersion Correction (DFT-D) for the 94 Elements H-Pu. *J. Chem. Phys.* **2010**, *132*, 154104.
(42) Blöchl, P. E. Projector Augmented-Wave Method. *Phys. Rev. B: Condens. Matter Mater. Phys.* **1994**, *50*, 17953−17979.
(43) Henkelman, G.; Arnaldsson, A.; Jónsson, H. A Fast and Robust Algorithm for Bader Decomposition of Charge Density. *Comput. Mater. Sci.* **2006**, *36*, 354−360.
(44) Sanville, E.; Kenny, S.; Smith, R.; Henkelman, G. An Improved Grid-Based Algorithm for Bader Charge Allocation. *J. Comput. Chem.* **2007**, *28*, 899−908.
(45) Tang, W.; Sanville, E.; Henkelman, G. A Grid-Based Bader Analysis Algorithm without Lattice Bias. *J. Phys.: Condens. Matter* **2009**, *21*, No. 084204.
(46) Yu, M.; Trinkle, D. R. Accurate and Efficient Algorithm for Bader Charge Integration. *J. Chem. Phys.* **2011**, *134*, No. 064111.
(47) Lei, N.; Huang, Z.; Rice, S. A. Surface Segregation and Layering in the Liquid−Vapor Interface of a Dilute Bismuth-Gallium Alloy. *J. Chem. Phys.* **1996**, *104*, 4802−4805.

DOI: 10.1021/acscatal.9b01833
ACS Catal. 2019, 9, 8337−8345